

Removal of spatial biological artifacts in functional maps by local similarity minimization

Tomer Fekete^{a,b,*}, David B. Omer^{a,1}, Shmuel Naaman^a, Amiram Grinvald^a

^a Department of Neurobiology, The Weizmann Institute of Science, 76100 Rehovot, Israel

^b The Interdisciplinary Center for Neural Computation, The Hebrew University, 91904 Jerusalem, Israel

ARTICLE INFO

Article history:

Received 11 February 2008

Received in revised form 23 October 2008

Accepted 12 November 2008

Keywords:

Noise reduction

Functional maps

Blood vessels

f-MRI

Optical imaging

Voltage-sensitive dye

Intrinsic imaging

ABSTRACT

Functional maps obtained by various technologies, including optical imaging techniques, f-MRI, PET, and others, may be contaminated with biological artifacts such as vascular patterns or large patches of parenchyma. These artifacts originate mostly from changes in the microcirculation that result from either activity-dependent changes in volume or from oximetric changes that do not co-localize with neuronal activity per se. Standard methods do not always suffice to reduce such artifacts, in which case conspicuous spatial artifacts mask details of the underlying activity patterns. Here we propose a simple algorithm that efficiently removes spatial biological artifacts contaminating high-resolution functional maps. We validated this procedure by applying it to cortical maps resulting from optical imaging, based either on voltage-sensitive dye signals or on intrinsic signals. To remove vascular spatial patterns we first constructed a template of typical artifacts (vascular/cardiac pulsation/vasomotion), using principle components derived from baseline information obtained in the absence of stimulation. Next, we modified this template by means of local similarity minimization (LSM), achieved by measuring neighborhood similarity between contaminated data and the artifact template and then abolishing the similarity. LSM thus removed spatial patterns originating from the cortical vasculature components, including large fields of capillary parenchyma, helping to unveil details of neuronal activity patterns that were otherwise masked by these vascular artifacts. Examples obtained from our imaging experiments with anesthetized cats and behaving monkeys showed that the LSM method is both general and reproducible, and is often superior to other available procedures.

© 2008 Elsevier B.V. All rights reserved.

1. Introduction

Optical imaging of intrinsic signals in vivo (Grinvald et al., 1986) and in vivo optical imaging of voltage-sensitive dye signals (Grinvald et al., 1984; Grinvald and Hildesheim, 2004) are powerful techniques for visualizing the functional architecture of large neuronal populations or their intricate dynamics. High-resolution functional maps were also obtained recently (Yacoub et al., 2008; Cheng et al., 2001) by BOLD f-MRI (Ogawa et al., 1992).

During high-resolution optical imaging, functional maps (Blasdel and Salama, 1986; Katz et al., 1989; Tso et al., 1990; Frostig et al., 1990; Bonhoeffer and Grinvald, 1993; Fitzpatrick, 1996; Sheth et al., 1996; Weliky et al., 1996) are obtained by a step-wise procedure. First, optical data are normalized by the pattern of

illumination (the static aspects of the preparation and illumination, which are picked up by the imaging device and remain unchanged during imaging). Next, the results of trials carried out under the same stimulus conditions are averaged. Finally, a functional map (or differential map) is obtained by subtracting the average for one stimulus condition from the average for another condition (for a detailed technical review see Grinvald et al., 1999).

The optical signal results primarily from five sources: (a) stimulus-related neuronal activity; (b) spontaneous neuronal activity; (c) changes in cortical vasculature and parenchyma owing to heart pulsations and respiration; (d) “vasomotion”, noise that appears like patches moving around at 0.1 Hz (Mayhew et al., 1996); (e) various other types of noise, such as that caused by cortical motion. Sufficient averaging should remove some types of noise and spontaneous activity that are not stimulus-locked. Accordingly, the averaged data should contain the characteristic biological artifacts captured by the imaging setup, such as vascular artifacts related to heartbeat and respiration. Differential imaging may then achieve near-complete elimination of biological artifacts, because whenever both averaged maps contain similar artifact residues they can be removed by simple subtraction.

* Corresponding author at: Department of Neurobiology, The Weizmann Institute of Science, P.O. Box 26, 76100 Rehovot, Israel. Tel.: + 972 8 9343833; fax: +972 8 9342438.

E-mail address: tomer.fekete@weizmann.ac.il (T. Fekete).

¹ These authors contributed equally to this work.

Conventional methods are not always satisfactory, however, and functional maps may then exhibit conspicuous biological artifacts, especially in regions of the imaged neuronal tissue that are traversed by large veins. It is well known that some vascular responses are actually stimulus specific, and will therefore not be eliminated by differential imaging. This is particularly obvious in functional maps of ocular dominance columns, where vascular artifacts are often reproduced in multiple repeated imaging sessions of the same cortical area (for a typical example see Fig. 1 in Tso et al., 1990).

The failure of standard methods to remove these vascular artifacts suggests either that the underlying assumption, namely that the biological processes giving rise to the noise are stationary across experimental conditions, was violated or that insufficient data were collected and therefore the noise estimates obtained are unreliable.

Numerous methods, based either on principal component analysis (PCA) (Mittra and Pesaran, 1999; Gabbay et al., 2005; Stetter et al., 2000) or source separation (Schiessl et al., 2000; Yokoo et al., 2001; Reidl et al., 2007), have been used in attempts to overcome the artifact problem. Here we suggest a simple approach which, unlike the abovementioned approaches, is biologically inspired, and thus is more successful at times in abating vascular artifacts. We assume that such noise, owing to the nature of the mechanisms giving rise to it, has a predictable form. Accordingly, we propose a computational scheme that estimates vascular artifacts using data collected in the absence of stimulation, by carrying out local (neighborhood) computations. This estimate can then be used to cleanse functional maps, revealing patterns of neuronal activity hitherto masked by vascular artifacts.

2. Materials and methods

All surgical and experimental procedures were in accordance with the National Institutes of Health guidelines. All data were analyzed by MATLAB (www.mathworks.com, version 7.1).

2.1. Analysis of optical imaging data

The data used for validating the proposed analysis procedure were obtained by voltage-sensitive dye imaging and by intrinsic imaging. All of the imaging data were obtained from the primary cortices of awake primates and of anesthetized cats (for detailed methods see Bonhoeffer and Grinvald, 1993; Grinvald et al., 1999; Slovín et al., 2002).

We used two experimental paradigms to produce functional maps of ocular dominance and of orientation preference. The ocular dominance paradigm should provide identical stimuli containing all possible visual attributes to each eye separately. In our simplified imaging paradigm we varied the experimental conditions by presenting each animal with several different stimuli: (a) a full-field oriented moving square-wave grating of 0° (“ 0° stimulus”) to the right eye; (b) a 90° stimulus to the right eye; (c) a 0° stimulus to the left eye; (d) a 90° stimulus to the left eye; (e) no visual stimulation (baseline data).

In the orientation preference (“orientation”) paradigm the experimental conditions for imaging were the following: (a) a 0° stimulus presented to both eyes; (b) a 90° stimulus, both eyes; (c) no visual stimulation (baseline data). More elaborate stimulation paradigms exist, and we verified that the LSM algorithm described below is not sensitive to the way in which a functional map is obtained.

2.2. Local similarity minimization (LSM)

In this section we describe the method we devised to eliminate spatial vascular artifacts in functional maps. A schematic representation and general outline are given in Fig. 1.

Our strategy in tackling these artifacts was to attempt to estimate the artifacts present in the evoked patterns through local analysis. Our underlying assumption was that vascular artifacts share a “family resemblance”, i.e., common global features that

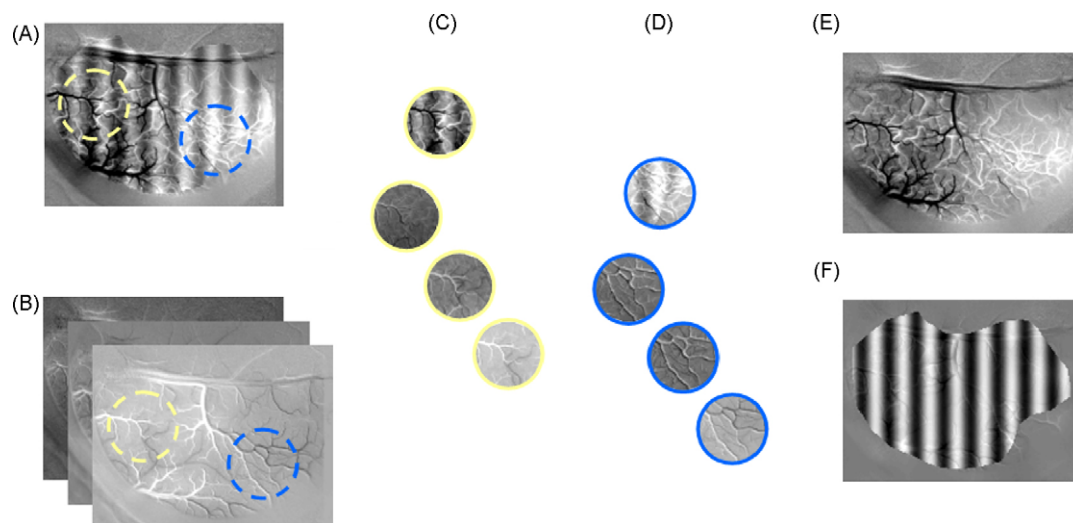


Fig. 1. Schematic illustration of the local similarity minimization (LSM) algorithm. The LSM algorithm estimates the biological artifacts corrupting functional maps for each pixel independently, using its local surroundings and additional information about the artifacts. (A) A simulated contaminated functional map. The source for estimation of the artifact is the “baseline” data (data collected in the absence of stimuli). Singular value decomposition (SVD) is used to derive templates spanning the “artifact space”. (B) The first three principal components given by the SVD of the baseline data were used to produce the simulated contaminated functional map shown in (A). (C) To estimate the artifact for the central pixel in the image sub-region in (A) marked by a yellow dashed line (the map neighborhood), the corresponding neighborhoods in the principal components in (B) (the noise neighborhoods) are considered. These neighborhoods are shown in (C). Next, the similarity (e.g. the dot product) between the marked sub-image of the contaminated functional map in (A) and the corresponding sub-images of the artifact templates (i.e., B) is abolished: a weighted sum of the noise neighborhoods is subtracted from the map neighborhood. The similarity between the cleansed neighborhood and each noise neighborhood is now 0. The value obtained for the central pixel is stored. (D) The procedure is repeated for all other pixels independently. Here it is shown for another pixel—the central pixel of the sub-image of the map in (A) marked by a blue dashed line. (E) Application of the same computation for all pixels yields a global estimate of the artifact. (F) The estimate of the actual artifact shown in (E) is subtracted from the contaminated map shown in (A), resulting in near-complete elimination of the artifact corrupting the map.

vary locally. This was a reasonable assumption, given that stimulus-dependent vascular activity, while produced throughout the entire vascular bed, is modulated locally according to different underlying neuronal activities that interact locally with the neighboring microvascular tree. Such activity, moreover, produces continuous effects in space. Therefore, if a suitable template of the typical vascular changes can be continuously modified locally by the use of local measurements of the contaminated data, it might result in a more reliable estimate of the activity-dependent vascular response. The first step towards achieving this would be to compute a template of the typical vascular artifacts.

To this end, we utilize the baseline data obtained in the absence of stimuli. These data reflect several types of activity: spontaneous neuronal activity, spontaneous vascular activity, vascular changes originating from cardiac pulsation and respiration, and noise. If such data (triggered on the ECG trace in the case of voltage-sensitive dye imaging) are sufficiently averaged the resulting image set contains

the typical cardiac/vascular activity in each patch of imaged cortex, since the other types of activities – patterns of spontaneous neuronal activity and spontaneous vascular activity patterns, as well as noise – average out. To achieve further de-noising of the baseline data as well as computational efficiency (by dimensionality reduction) **singular value decomposition** (SVD, Golub and Van Loan, 1996) of the baseline images stacked as vectors (column by column) is carried out. The first K principal components produced by SVD of the baseline data, the set $\{V_1 \dots V_K\}$ of orthonormal vectors – each of which is an image – are taken as the templates of the vascular artifacts.

The next step is to modify the artifact templates locally, pixel by pixel, to obtain an estimate of the activity-dependent artifact. This estimate can be subtracted from the contaminated image to produce a cleansed image. The objective is to minimize a similarity measure between a small region (“neighborhood”) surrounding each pixel in the cleansed image and the corresponding areas

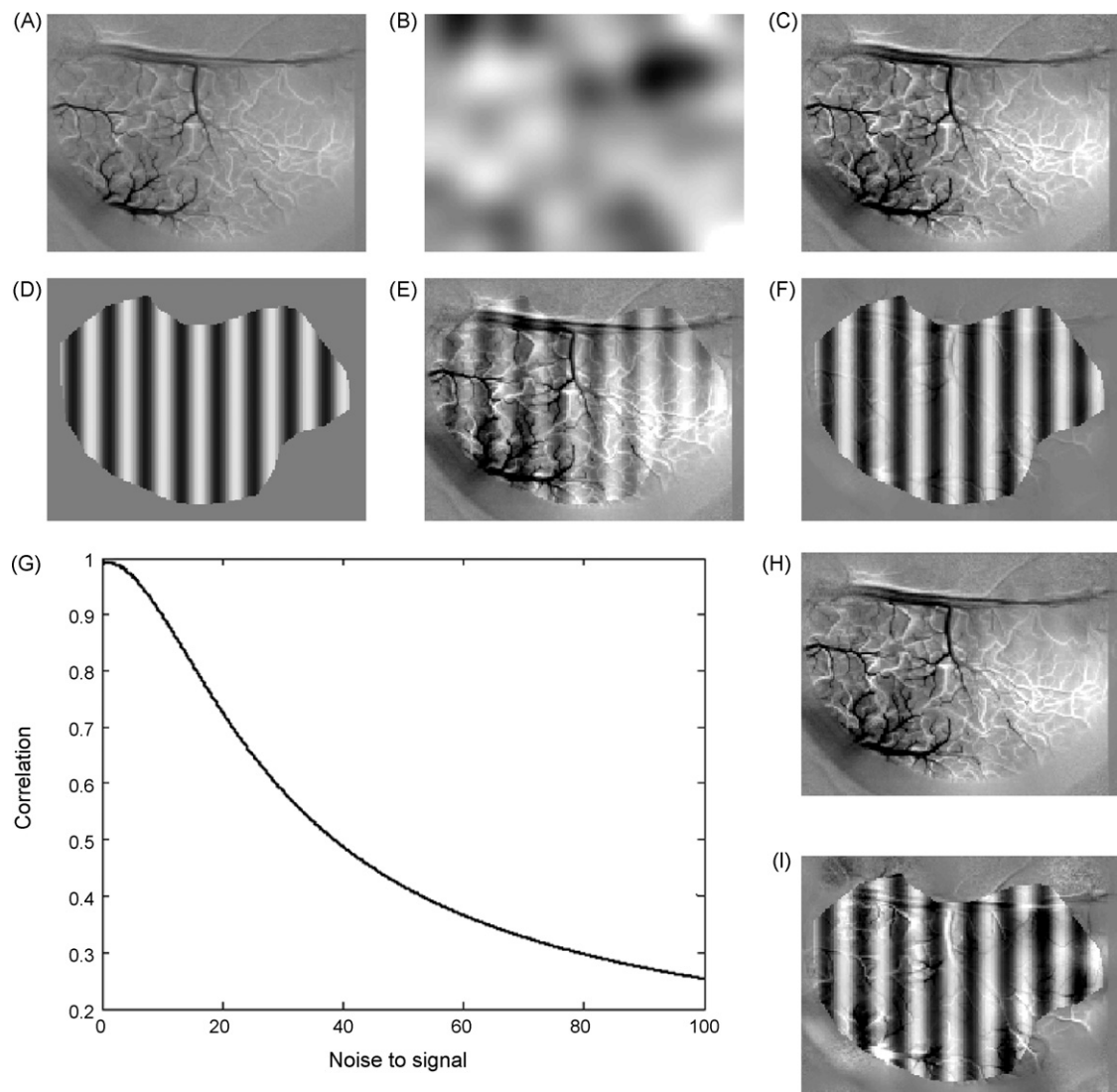


Fig. 2. Synthetic example depicting the performance of the LSM algorithm. (A) A vascular pattern, composed of a random combination of three principal components, produced by SVD of the baseline data. Baseline data were obtained by imaging the cortex without a stimulus. (B) A smooth gradient (see text), representing non-specific modifications in vascular reflectance that originate from “vasomotion”. (C) The artifact pattern resulting from point-by-point multiplication of the noise patterns shown in (A) and (B). (D) An artificial functional map pattern (signal pattern). (E) A combination of the artifact pattern shown in (C) with the functional map shown in (D). (F) Output of the LSM algorithm applied to the simulated contaminated functional map shown in (E). Both this map and the baseline data were given as input. The output exhibits high correlation (0.99) with the original uncontaminated functional map pattern (compare F and D). (G) These steps are repeated while varying the ratio between the standard deviations of the artifact pattern (C) and the signal pattern (D). The quality of reconstruction, as measured by the correlation of the LSM-cleansed images with the original pattern (D), is plotted as a function of the amount of noise (the abovementioned ratio). The example seen in (E) corresponds to a noise level of 1.9. (H and I) Same as (E), (F), but for a noise level of 10.

in each of the images comprising the vascular artifact templates. Accordingly, we refer to the described algorithm as **"local similarity minimization"** (LSM). The similarity measure we found most effective for this purpose is the Euclidean dot product (results not shown).

We denote the radius (r)-sized neighborhood of the $n \times m$ original image Im surrounding the i th pixel (i designating a pixel's index when the image is taken as a vector) as $\text{Im}^{(i,r)}$. $\text{Im}^{(i,r)}$ would be the $(r+1) \times (r+1)$ sized sub-image of Im in which the center pixels is i . Similarly the corresponding neighborhoods of the artifact templates are denoted as $V^{(i,r)} = [V_1^{(i,r)} \dots V_j^{(i,r)} \dots V_K^{(i,r)}]$. We wish to find a vector of weights $a^{(i,r)} = [a_1^{(i,r)} \dots a_j^{(i,r)} \dots a_K^{(i,r)}]^T$ for the artifact templates, such that if this weighted sum is removed from the contaminated image in the neighborhood of pixel i , the similarity between the resulting neighborhood and the corresponding neighborhoods of the artifact templates will be 0. That is to say:

$$\text{for each } V_j, \quad \langle \text{Im}^{(i,r)} + V^{(i,r)} A^{(i,r)}, V_j^{(i,r)} \rangle = \left(\text{Im}^{(i,r)} + \sum_{k=1}^K a_k^{(i,r)} V_k^{(i,r)} \right)^T V_j^{(i,r)} = 0. \quad (1)$$

Using the symmetry of the inner product, Eq. (1) can be written in matrix form thus

$$(V^{(i,r)})^T (\text{Im}^{(i,r)} + V^{(i,r)} a^{(i,r)}) = 0. \quad (2)$$

Rearranging the terms results in the following linear system of equations:

$$C^{(i,r)} a^{(i,r)} = -C_{\text{Im}}^{(i,r)}, \quad (3)$$

where $C^{(i,r)}$, the coefficient matrix, is the inner product matrix:

$$C^{(i,r)} = \langle V^{(i,r)}, V^{(i,r)} \rangle = (V^{(i,r)})^T V^{(i,r)};$$

$$C_{\text{Im}}^{(i,r)} = \langle V^{(i,r)}, \text{Im}^{(i,r)} \rangle = (V^{(i,r)})^T \text{Im}^{(i,r)} \text{ is the solution vector.}$$

To realize the local scheme, the above computation is solved for each pixel independently and the result stored. The scheme can be efficiently implemented via convolution with a mask (the matrix representation of the convoluting function) supported (i.e., receiving non-zero values) in a radius (r)-sized neighborhood. Rather than using a rectangular binary mask, we chose to use a smoothly decaying round mask to avoid introducing artifacts (edge effects) in the estimated noise image. The mask we used was a Butterworth type (Rabiner and Gold, 1975, and see equation below), as the profile

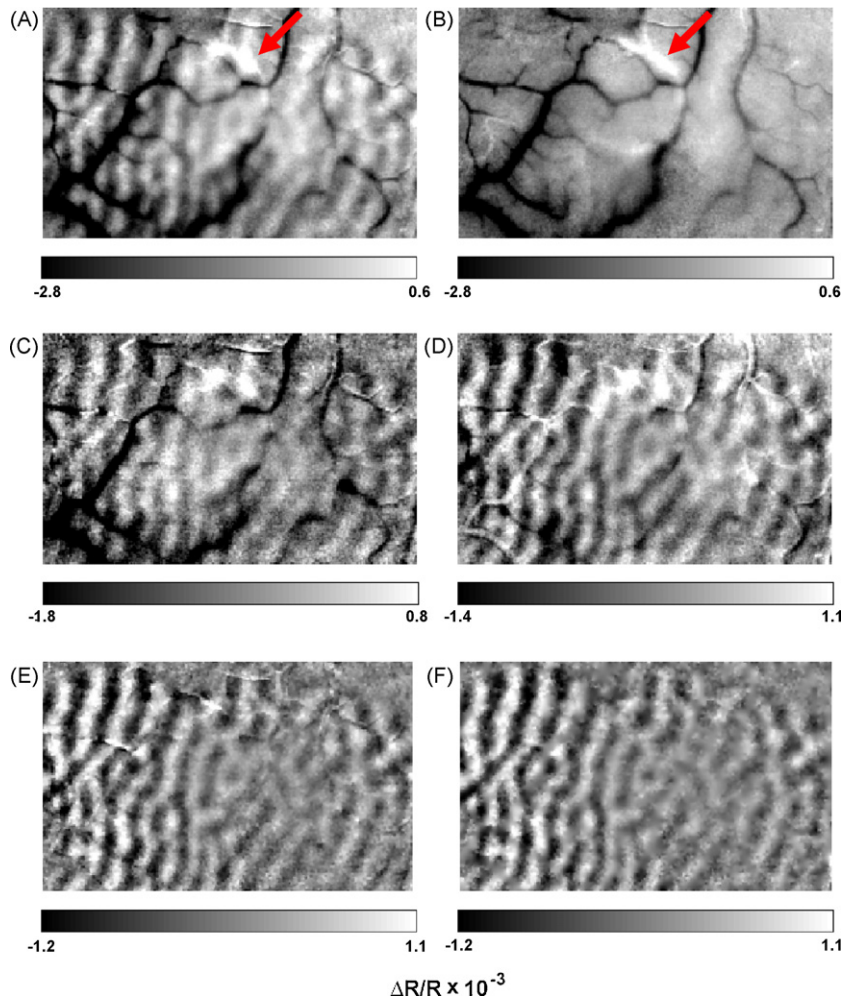


Fig. 3. LSM outperforms other methods in eliminating vascular artifacts. (A) An ocular-dominance functional map obtained by intrinsic imaging of the primary visual cortex in an awake primate. This map was obtained by differential imaging. (B) The artifact as estimated by LSM. Note that not only vessels but also patches are picked up; see red arrows in (A) and (B). (C) The ocular-dominance map computed after independent component analysis (ICA) via the FastICA algorithm (Hyvärinen, 1999). (D) The map produced after application of the GIF method (Yokoo et al., 2001). (E) The map produced by LSM. (F) The map in (E) after **radial basis function (RBF) smoothing**. Elimination of vascular and patchy artifacts is far superior to that accomplished by the methods used to obtain the functional maps in (C) and (D), in which vascular artifacts persist.

of such functions is a smooth approximation of a discrete (square) cutoff. Thus, the linear system of equations (Eq. (3)) is assembled as follows:

- (a) A smooth approximation of a round binary mask of radius r , the $n \times m$ matrix $B^{(r)}$ given by Eq. (4), is constructed:

$$B^{(r)}(x, y) = \frac{1}{1 + (d(x', y')/s)^{12}}, \quad (4)$$

where d is the Euclidean norm of the centered (x, y) coordinates (i.e., the pixel indices), $x' = (x - 1) - 0.5(x_{\max} - 1)$, and likewise for y . The mask is matched with a suitable parameter s

to produce a circular mask of radius r (i.e. $B^{(r)}(0, r) = 0.95$):

$$s = 1.2781r. \quad (5)$$

- (b) Taking both the contaminated map and artifact templates as matrices, the inner product matrices are assembled for all template pairs:

$$C_{jk}^{(r)} = \frac{1}{r} [V_j \times V_k] \otimes B^{(r)}, \quad (6)$$

where \times denotes element-by-element matrix multiplication. The image-to-template products are similarly computed:

$$C_{lm,j}^{(r)} = [I_{lm} \times V_j] \otimes B^{(r)}. \quad (7)$$

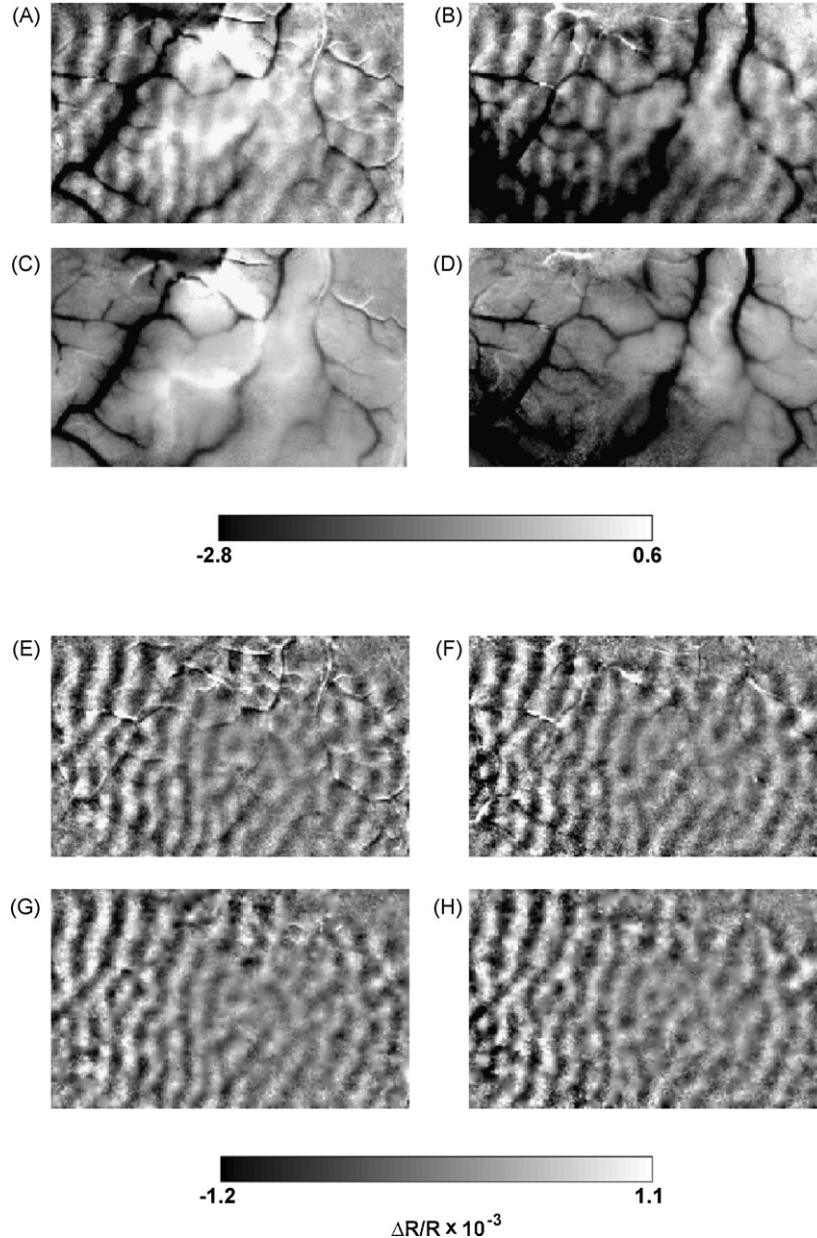


Fig. 4. High reproducibility obtained with LSM. The data that were used to produce the ocular-dominance map in Fig. 3A were divided into two independent halves, and two independent ocular-dominance maps were computed, yielding two test maps. LSM was applied to each of the two test maps separately. (A and B) The two ocular-dominance maps computed from the two halves of the data set of Fig. 3A. Correlation of the test maps to the map produced from the entire data (Fig. 3A) was about 0.83 in both cases, while the correlation between the test maps was only 0.4, indicating that the artifacts were not averaged out. (C) The artifact estimated by LSM for the test map shown in (A). (D) LSM-estimated artifact for the test map shown in (B). Note the substantial differences between (C) and (D). (E and F) The test maps cleansed by LSM. (E) The test map in (A) after cleansing by LSM. (F) The test map in (B) after cleansing by LSM. Correlations between the LSM-cleansed maps with the LSM-cleansed map produced from the entire data (Fig. 3E), increased to about 0.85 in both cases. (G) The same map as in (E) after RBF smoothing. (H) The same map as in (F) after RBF smoothing. Correlation of the maps in (G) and (H) with the respective map produced for the entire data (Fig. 3F) was about 0.9 in both cases.

- (c) The coefficient matrices are formed for each pixel by stacking the coefficients $C_{jk}^{(i,r)}$ in the appropriate order, and similarly for the solution vectors.

2.3. Radial basis function (RBF) smoothing

If necessary, the cleansed image can be further improved by smoothing only those regions of the image that contain blood vessels, using compactly supported radial basis functions (RBFs; see [Mathematical Appendix](#) and [Wendland, 1995](#)). A mask of the vasculature (i.e. a binary image in which the vasculature pattern appears) is computed and the remaining points are used to compute the coefficients. A comparison between the results obtained with LSM + RBF smoothing and with LSM alone is shown in [Supplementary Fig. 2](#). The computation time can be shortened by the use of methods described in [Morse et al. \(2001\)](#) and [Ohtake et al. \(2003\)](#).

3. Results

3.1. A synthetic example

To test both our underlying assumptions and the LSM algorithm, we generated artificial contaminated images ([Fig. 2A–E](#)). We tried to mimic the phenomena seen in real data (and, with intrinsic imaging, often in real time when utilizing real-time enhanced differential imaging; see [Fig. 13](#) in [Grinvald et al., 1999](#)). Observe, for example, the contaminated functional map in [Fig. 3A](#). The map is blemished by blood vessels. Moreover, around the blood vessels there are dark and light patches of a lower spatial frequency, similar to what was directly visualized with real-time differential imaging, i.e., the 0.1 Hz vasomotion noise ([Mayhew et al., 1996](#)). Accordingly, in order to mimic this scenario, the vascular pattern could be modulated by means of low frequency spatial modulation and added to a synthetic functional pattern.

To simulate a vascular pattern undergoing low frequency, or “patchy”, modulations, we first took actual images of vascular pat-

terns obtained from the SVD of a baseline data set (see [Section 2](#)) to serve as the vascular artifact templates. In the example shown in [Fig. 2A](#), the first three principal components produced by SVD of the baseline data were summed (with arbitrary coefficients). The resulting image was multiplied, point by point, by a smooth gradient ([Fig. 2B](#)). The gradient was produced by low-pass filtering and adjustment of 2D noise images (sampled randomly from a uniform distribution) to attain a distribution of values between 1 and 3. Therefore, when multiplied by this patchy pattern some of the values in the original vasculature pattern were increased up to threefold (points in [Fig. 2A](#) multiplied by areas in the gradient corresponding to light patches in [Fig. 2B](#)), while others remained almost unchanged (points in [Fig. 2A](#) multiplied by areas in the gradient corresponding to dark areas in [Fig. 2B](#)). This modification of the vascular pattern represents the local changes in vascular activity that characterize the biological artifacts seen in functional maps, some of which originate from the abovementioned low-frequency 0.1 Hz vasomotion noise ([Mayhew et al., 1996](#)). The resulting image, the “artifact” pattern, is shown in [Fig. 2C](#). Finally a “signal” pattern, a sinusoidal grating mimicking an ocular-dominance functional map pattern ([Fig. 2D](#)), was added to produce a “contaminated” image ([Fig. 2E](#)).

Both the contaminated image ([Fig. 2E](#)) and baseline data were given as input. The LSM algorithm achieved a near-perfect reconstruction of the signal (compare the result in [Fig. 2F](#) to the input in [Fig. 2D](#)). The quality of the reconstruction was assessed in terms of the correlation of the reconstructed pattern ([Fig. 2F](#)) with the signal pattern ([Fig. 2D](#), $r = 0.99$).

To assess the sensitivity of LSM to the signal-to-noise ratio, we varied the ratio between the standard deviation of the artifact pattern ([Fig. 2C](#)) and the signal pattern ([Fig. 2D](#)), and applied LSM in each case. A plot of the correlation of the cleansed pattern produced by LSM with the signal pattern as a function of the noise level (the abovementioned ratio) is shown in [Fig. 2G](#). The example shown in [Fig. 2E](#) corresponds to a noise level of 1.9. The example in [Fig. 2H](#) contains a noise level of 10, and at this much higher noise the signal

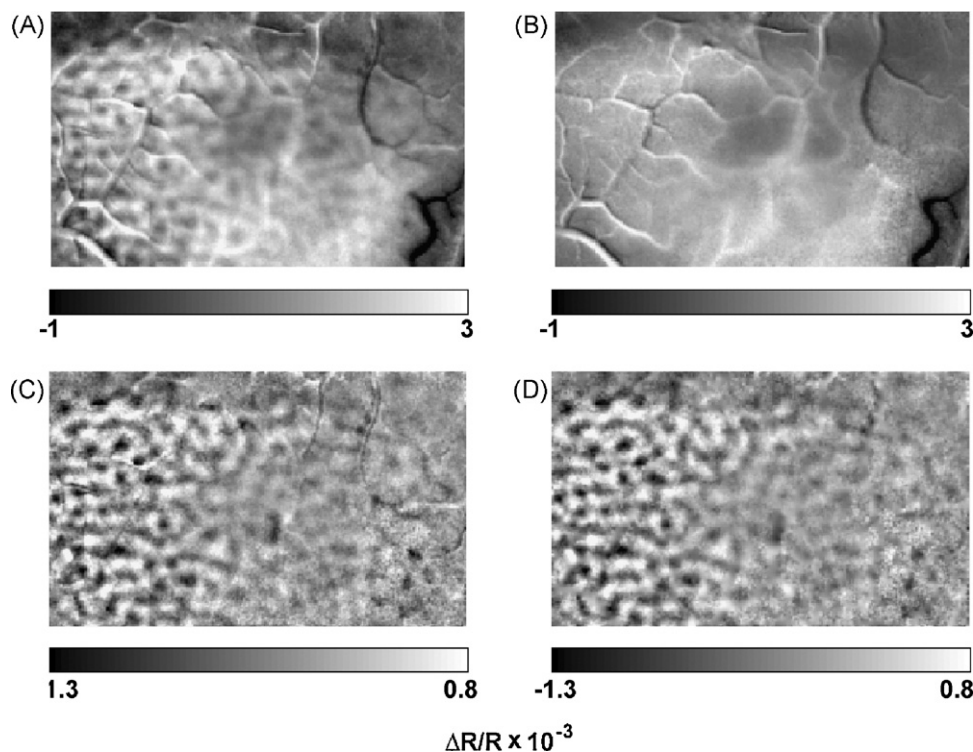


Fig. 5. Improvement of an orientation-preference map by LSM. (A) Original orientation map obtained by intrinsic imaging from the primary visual cortex of an awake primate. (B) Estimate of the artifact by LSM. (C) Cleansed image produced by LSM. (D) Cleansed image (in C) after RBF smoothing.

pattern is hardly seen. The resulting uncontaminated signal pattern, shown in Fig. 2I, demonstrates the efficient performance of the LSM algorithm on this type of noise in the simulated data (compare the map in Fig. 2I to that hidden in the noisy data of Fig. 2H).

3.2. Cleansing functional maps: comparison with other methods

For clarity we will focus initially on one example, in which intrinsic signals were imaged from the primary visual cortex of an awake primate in order to produce an ocular dominance functional map (Figs. 3 and 4).

Fig. 3 shows the comparison of LSM both with the method of independent component analysis (ICA; Cardoso, 1999; Hyvärinen, 1999; also see Reidl et al., 2007 for application of ICA to voltage-sensitive dye imaging data) and with the generalized indicator function method (GIF, Yokoo et al., 2001). In the results presented below we used a 7 pixels radius neighborhood for LSM and either 5 or 10 principal components (depending on the number of frames captured during the baseline trials). The RBF used was $(1 - r)_+^2$ (see Appendix A) and the radius of support was 13 pixels.

The results showed that LSM outperformed these methods. ICA (either the FastICA of Hyvärinen, 1999 or the JadeR algorithm of Cardoso, 1999) was not useful in abating the vascular noise (see Fig. 3C), while the GIF method (Fig. 3D) proved less effective than LSM, in terms of both the residual blood vessels that remained after the algorithms were applied, and the residual non-specific low-frequency variation (see Supplementary Fig. 1; compare the vascular artifacts seen in the functional maps shown in Fig. 3C and D with those obtained by means of the LSM algorithm).

3.3. Reproducibility of LSM

To demonstrate the reproducibility of the LSM algorithm we divided our case-study data in half to produce two independent ocular-dominance functional maps (Fig. 4A and B), which we will refer to as “test maps”.

The correlation of these two test maps with the ocular dominance map produced from the entire data (Fig. 3A) was 0.83 for Fig. 4A and the same for Fig. 4B. The correlation between the two test maps themselves (Fig. 4A and B) was only about 0.4. These correlations increased after application of LSM: correlations of the cleansed maps with the map produced from the entire data and cleansed by LSM (Fig. 3E) were 0.85 (Fig. 4E) and 0.86 (Fig. 4F). RBF smoothing of the LSM-cleansed test maps further increased their correlations with the cleansed and smoothed ocular-dominance map produced from the entire data (Fig. 3F) to 0.89 (Fig. 4G) and 0.9 (Fig. 4H). Visual inspection of the images depicted in Fig. 4 indeed shows that the LSM algorithm, with or without RBF smoothing, is highly reproducible.

3.4. Additional examples

We next applied LSM to an intrinsic imaging orientation preference map obtained from the primary visual cortex (V1) of a behaving primate. The result, seen in Fig. 5, shows that vascular artifacts were successfully eliminated.

Another example, depicting an orientation-preference map obtained from voltage-sensitive dye imaging of V1 of an anesthetized cat (Fig. 6), also shows marked improvement after the LSM algorithm was applied.

Finally, we applied LSM to a voltage-sensitive dye imaging ocular-dominance map obtained from V1 of a behaving primate. The result is shown in Fig. 7.

As the figure again clearly shows, the functional map obtained after LSM application (Fig. 7C) is superior to the raw map depicted

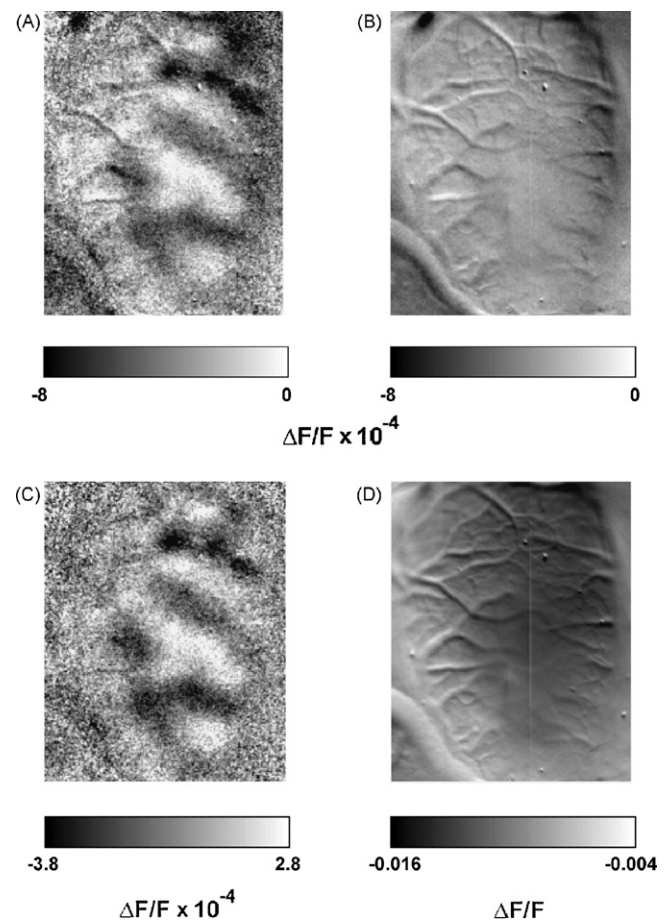


Fig. 6. Improvement of a voltage-sensitive dye imaging orientation-preference map by LSM. (A) Original orientation map obtained by voltage-sensitive dye imaging of the primary visual cortex of an anesthetized cat. (B) Estimate of the artifact by LSM. (C) Cleansed image produced by LSM. (D) Average baseline pattern produced in the absence of stimulation.

in Fig. 7A, in which the viewer cannot be certain that an ocular-dominance functional map was indeed imaged.

3.5. Computational efficacy of LSM

Two parameters are needed for LSM—the neighborhood radius (r) and the number of principal components (K). The neighborhood size required depends on the resolution of the camera used for imaging, the size of functional domains, and the amount of zoom-in. It is therefore a characteristic of the imaging setup. Moreover, the number of principal components can be selected automatically by setting a predefined threshold for the percentage of variance in the baseline data to be accounted for by these components. Thus, after initial calibration, LSM can be fully automated. In all analyzed cases that originated from the same experimental setup we indeed used the same parameters.

LSM is also computationally efficient; its overall computational complexity is bounded by $O(n^2 \times \sqrt{n})$ (see Appendix A), where n denotes the number of pixels in each image. To determine the actual speed of LSM, we carried out computations on random square matrices. In all cases the “baseline” data comprised 50 random images, and the first five principal components derived from these data were decorrelated from the random “contaminated” image in each case. The machine the tests were run on was fitted with a Dual core AMD Opetron 280 2.4 GHz processor and 8 GB REM. The results are shown in Table 1.

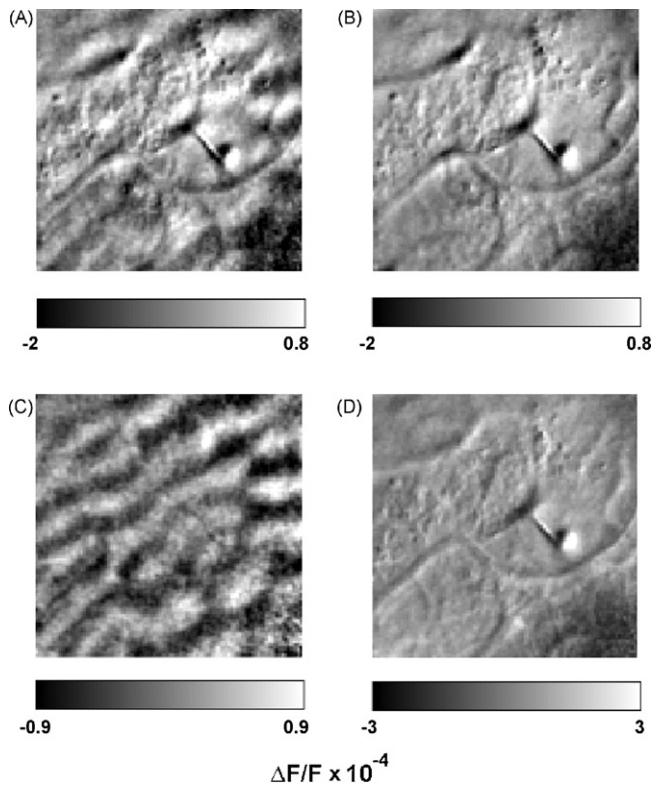


Fig. 7. Improvement of a voltage-sensitive dye imaged ocular-dominance map by LSM. (A) Original ocular-dominance map obtained by voltage-sensitive dye imaging of the primary visual cortex of an awake primate. (B) Estimate of the artifact by LSM. (C) Cleansed image produced by LSM. (D) Average baseline pattern produced in the absence of stimulation.

4. Discussion

We devised a method, which we termed “local similarity minimization” (LSM), which allows spatial biological artifacts to be eliminated from functional maps. We validated the method by applying it to contaminated maps produced by functional optical-imaging techniques. The LSM algorithm proved quite effective in eliminating vascular artifacts, as seen in Figs. 3–7. The method proved superior to some well-established methods, such as ICA and the GIF method (Fig. 3). Furthermore LSM was found to be computationally efficient, and does not require delicate tweaking of parameters. It is also highly reproducible.

By selecting results from relatively poor experiments that were previously discarded, we showed here that the LSM algorithm can salvage inferior yet expensive data that would otherwise be useless.

A number of methods based on local analysis have been proposed in the past for medical image analysis and sequence analysis (e.g. Furlanello and Giuliani, 1995; Ma et al., 2005), and share some superficial resemblance to our method. However, our approach contains three novel aspects: (a) the optimization criterion, namely

the local decorrelation to the linear subspace spanned by the baseline templates; (b) implementation via convolution; (c) the use of a smoothly decaying circular mask (i.e. convolving function) to avoid artifacts.

The assumptions underlying the LSM algorithm are biologically motivated. Accordingly, the proposed method is widely applicable; we demonstrate its usefulness here in both intrinsic optical imaging and voltage-sensitive dye optical imaging. Further still, using this approach it will apparently also be possible to remove non-biological noise, as long as it does not vary with the stimulus. Hence, this method should be helpful to scientists working on functional mapping of the mammalian cortex, using other methodologies, as well as to others in diverse scientific fields.

Acknowledgments

We thank Rina Hildesheim for dyes and Yuval Toledo for computer technical assistance. TF wishes to thank Neta Zach, as well as Hagai Lalazar, for helpful discussions and comments on the manuscript. This work was supported by The Weizmann Institute of Science, Rehovot, Israel, and an EU Daisy grant.

Appendix A. Radial basis functions (RBFs)

Two-dimensional (2D) radial basis functions are polynomials of the Euclidian distance from center points, i.e., $\phi(x, y) = P(r)$, where P is a polynomial, and $r = \sqrt{(x - x_0)^2 + (y - y_0)^2}$, i.e., ϕ is centered around (x_0, y_0) . We say that ϕ is compactly supported if it receives non-zero values in a compact neighborhood centered around (x_0, y_0) , in the above setting the closed circle of radius r .

The bending energy **bE** of a function $f(x, y)$, which is given by

$$\mathbf{bE}(f) = \int_y \int_x \left(\frac{\partial^2 f}{\partial x^2} \right)^2 + 2 \left(\frac{\partial^2 f}{\partial x \partial y} \right)^2 + \left(\frac{\partial^2 f}{\partial y^2} \right)^2$$

is a measure of a surface's smoothness (Costa and Cesar, 2001). RBFs that minimize bending energy can be derived and utilized to approximate scattered data. If k points (x_i, y_i, z_i) are sampled, and (x_i, y_i) are taken to be the centers of support for the functions ϕ_i , it is possible to derive a linear system of equations that will result in a function having the form $f(x, y) = a + a_x x + a_y y + \sum a_i \phi_i(x, y)$. The constraints $\sum a_i = 0$, $\sum a_i x_i = 0$, and $\sum a_i y_i = 0$ are added to ensure that the bending energy is minimized.

The reason for using compactly supported RBFs is that the ensuing system of equations can be made sparse by using a small radius of support, thereby reducing the computation time by a factor of \sqrt{n} (n being the size of the input data points) and the required storage by a factor of n (Morse et al., 2001). Computation is further facilitated if the approximation is carried through on overlapping smaller image segments and smoothly mixed by construction of a partition of unity (see, for example, Ohtake et al., 2003).

In our analysis we used the basis function of the form:

$$(1 - r)_+^2 = \begin{cases} \left(1 - \frac{d(x, c)}{r}\right)^2, & d < r, \\ 0, & d \geq r, \end{cases} \quad (\text{S1})$$

given in Wendland (1995).

4.1. Computational complexity of local similarity minimization (LSM)

LSM occurs in three stages: (a) computation of the singular value decomposition (SVD) of the baseline data; (b) building coefficient and solution matrices via convolution; (c) solving the system of equations. SVD theorem insures us that the principal components

Table 1
Computational efficacy of local similarity minimization.

Size (pixels)	Time (s) ^a
100 ²	0.4
300 ²	4.1
600 ²	13
800 ²	24
1200 ²	55

^a Values are runtimes in seconds of LSM on random square image data sets as a function of image dimensions.

can be derived through finding the eigenvectors of either the temporal or spatial second-order moment matrix (Golub and Van Loan, 1996). The number of images used to form the vascular artifact template typically ranges from 5 to 100, while the number of pixels is of the order of 100×100 . Therefore, if n is the number of pixels and m the number of images, m is bounded by \sqrt{n} . Thus the computational complexity of this stage is $O(n^2 \times \sqrt{n})$. The computational complexity of the second stage results from that of the 2D fast Fourier transform used to compute convolution. Therefore, the complexity of this stage is bounded by $O(n \log(\sqrt{n}))$. Finally, the system of equations is solved for each pixel. The number of principal components needed for LSM is small (typically about five images account for most of the variance of the baseline data), with the result that the size of the linear systems that need to be solved is orders of magnitudes smaller than the number of pixels. Therefore, the overall complexity of LSM is bounded by $O(n^2 \times \sqrt{n})$. Note that the principal components, as well as the both the matrix coefficient and the Butterworth mask, need be formed only once for each data set.

Appendix B. Supplementary data

Supplementary data associated with this article can be found, in the online version, at doi:10.1016/j.jneumeth.2008.11.020.

References

- Blasdel GG, Salama G. Voltage-sensitive dyes reveal a modular organization in monkey striate cortex. *Nature* 1986;321(6070):579–85.
- Bonhoeffer T, Grinvald A. The layout of iso-orientation domains in area 18 of cat visual cortex: optical imaging reveals a pinwheel-like organization. *J Neurosci* 1993;13(10):4157–80.
- Cardoso JF. High-order contrasts for independent component analysis. *Neural Comput* 1999;11(1):157–92.
- Costa L da F, Cesar Jr RM. Shape analysis and classification: theory and practice. CRC Press; 2001. p. 318–30.
- Cheng K, Waggoner RA, Tanaka K. Human ocular dominance columns as revealed by high-field functional magnetic resonance imaging. *Neuron* 2001;32:359–74.
- Fitzpatrick D. The functional organization of local circuits in visual cortex: insights from the study of tree shrew striate cortex. *Cerebral Cortex* 1996;6(3):329–41.
- Frostig RD, Lieke EE, Ts'o DY, Grinvald A. Cortical functional architecture and local coupling between neuronal activity and the microcirculation revealed by in vivo high-resolution optical imaging of intrinsic signals. *PNAS* 1990;87(16):6082–6.
- Furlanetto C, Giuliani D. Combining local PCA and radial basis function networks for speaker normalization. In: Girosi F, Makhoul J, Manolakis E, Wilson E, editors. Proceedings of the IEEE workshop on neural networks for signal processing, vol. V. New York: IEEE; 1995. p. 233–42.
- Gabbay M, Brennan C, Kaplan E, Sirovich L. A principal components-based method for the detection of neuronal activity maps: application to optical imaging. *Neuroimage* 2005;11:313–25.
- Golub GH, Van Loan FV. Matrix computations. 3rd ed. Baltimore, MD: The Johns Hopkins University Press; 1996. p. 69–75.
- Grinvald A, Anglister L, Freeman JA, Hildesheim R, Manker A. Real-time optical imaging of naturally evoked electrical activity in intact frog brain. *Nature* 1984;308(5962):848–50.
- Grinvald A, Lieke E, Frostig R, Gilbert CD, Wiesel TN. Functional architecture of cortex revealed by optical imaging of intrinsic signals. *Nature* 1986;324:361–4.
- Grinvald A, Shoham D, Shmuel A, Glaser DE, Vanzetta I, Shtoyerman E, et al. In-vivo optical imaging of cortical architecture and dynamics. In: Windhorst U, Johansson H, editors. Modern techniques in neuroscience research. Heidelberg: Springer-Verlag; 1999. p. A893–969.
- Grinvald A, Hildesheim R. VSDI: a new era in functional imaging of cortical dynamics. *Nat Rev Neurosci* 2004;5(11):874–85.
- Hubel DH, Wiesel TN. Brain mechanisms of vision. *Sci Am* 1979;241(3):150–62.
- Hyvärinen A. Fast and robust fixed-point algorithms for independent component analysis. *IEEE Trans Neural Networks* 1999;10(3):626–34.
- Katz LC, Gilbert CD, Wiesel TN. Local circuits and ocular dominance columns in monkey striate cortex. *J Neurosci* 1989;9(4):1389–99.
- Ma Z, Feng D, Wu HR. A neighbourhood evaluated adaptive vector filter for suppression of impulse noise in colour images. *Real-time Imag* 2005;11(5–6):403–16.
- Mayhew JE, Askew S, Zheng Y, Porrill J, Westby GW, Redgrave P, et al. Cerebral vasomotion: a 0.1-Hz oscillation in reflected light imaging of neural activity. *Neuroimage* 1996;4(3 Pt 1):183–93.
- Mitra PP, Pesaran B. Analysis of dynamic brain imaging data. *Biophys J* 1999;76:691–708.
- Morse BS, Yoo TS, Rheingans P, Chen DT, Subramanian KR. Interpolating implicit surfaces from scattered surface data using compactly supported radial basis functions. *Shape Model Int* 2001:89–98.
- Ogawa S, Tank DW, Menon R, Ellermann JM, Kim SG, Merkle H, et al. Intrinsic signal changes accompanying sensory stimulation: functional brain mapping with magnetic resonance imaging. *PNAS* 1992;89(13):5951–5.
- Ohtake EEY, Belyaev AG, Alexa, Turk G, Seidel HP. Multi-level partition of unity implicits. *ACM Trans Graph* 2003;22(3):463–70.
- Otsu N. A threshold selection method from gray-level histograms. *IEEE Trans Syst Man Cyber* 1979;9:62–6.
- Rabiner LR, Gold B. Theory and application of digital signal processing. Englewood Cliffs, NJ: Prentice-Hall; 1975. p. 227.
- Reidl J, Starke J, Omer DB, Grinvald A, Spors H. Independent component analysis of high-resolution imaging data identifies distinct functional domains. *Neuroimage* 2007;34(1):94–108.
- Schiessl I, Stetter M, Mayhew JE, McLoughlin N, Lund JS, Obermayer K. Blind signal separation from optical imaging recordings with extended spatial decorrelation. *IEEE Trans Biomed Eng* 2000;47:573–7.
- Sheth BR, Sharma J, Rao SC, Sur M. Orientation maps of subjective contours in visual cortex. *Science* 1996;274(5295):2110–5.
- Slovin H, Arieli A, Hildesheim R, Grinvald A. Long-term voltage-sensitive dye imaging reveals cortical dynamics in behaving monkeys. *J Neurophysiol* 2002;88(6):3421–38.
- Stetter M, Schiessl I, Otto T, Sengpiel F, Hubener M, Bonhoeffer T, et al. Principal component analysis and blind separation of sources for optical imaging of intrinsic signals. *Neuroimage* 2000;11:482–90.
- Ts'o DY, Frostig RD, Lieke EE, Grinvald A. Functional organization of primate visual cortex revealed by high resolution optical imaging. *Science* 1990;249(4967):417–20.
- Weliky M, Bosking WH, Fitzpatrick D. A systematic map of direction preference in primary visual cortex. *Nature* 1996;379(6567):725–8.
- Wendland H. Piecewise polynomial, positive definite and compactly supported radial functions of minimal degree. *Adv Comput Math* 1995;4:389–96.
- Yacoub E, Harel N, Ugurbil K. High-field fMRI unveils orientation columns in humans. *PNAS* 2008;105(30):10607–12.
- Yokoo T, Knight BW, Sirovich L. An optimization approach to signal extraction from noisy multivariate data. *Neuroimage* 2001;14(6):1309–26.